Ann Nucl Med (2013) 27:152–162
DOI 10.1007/s12149-012-0667-3

ORIGINAL ARTICLE

# MRI-guided attenuation correction in whole-body PET/MR: assessment of the effect of bone attenuation

**A. Akbarzadeh · M. R. Ay · A. Ahmadian · N. Riahi Alam · H. Zaidi**

Received: 2 June 2012 / Accepted: 11 November 2012 / Published online: 21 December 2012


**Abstract**
*Objective* Hybrid PET/MRI presents many advantages in comparison with its counterpart PET/CT in terms of improved soft-tissue contrast, decrease in radiation exposure, and truly simultaneous and multi-parametric imaging capabilities. However, the lack of well-established methodology for MR-based attenuation correction is hampering further development and wider acceptance of this technology. We assess the impact of ignoring bone attenuation and using different tissue classes for generation of the attenuation map on the accuracy of attenuation correction of PET data.

*Methods* This work was performed using simulation studies based on the XCAT phantom and clinical input data. For the latter, PET and CT images of patients were used as input for the analytic simulation model using realistic activity distributions where CT-based attenuation correction was utilized as reference for comparison. For both phantom and clinical studies, the reference attenuation map was classified into various numbers of tissue classes to produce three (air, soft tissue and lung), four (air, lungs, soft tissue and cortical bones) and five (air, lungs, soft tissue, cortical bones and spongeous bones) class attenuation maps.
*Results* The phantom studies demonstrated that ignoring bone increases the relative error by up to 6.8 % in the body and up to 31.0 % for bony regions. Likewise, the simulated clinical studies showed that the mean relative error reached 15 % for lesions located in the body and 30.7 % for lesions located in bones, when neglecting bones. These results demonstrate an underestimation of about 30 % of tracer uptake when neglecting bone, which in turn imposes substantial loss of quantitative accuracy for PET images produced by hybrid PET/MRI systems.
*Conclusion* Considering bones in the attenuation map will considerably improve the accuracy of MR-guided attenuation correction in hybrid PET/MR to enable quantitative PET imaging on hybrid PET/MR technologies.

**Keywords** PET/MRI · PET/CT · Attenuation correction · Tissue classification · Quantification

A. Akbarzadeh · M. R. Ay (✉) · A. Ahmadian · N. Riahi Alam
Department of Medical Physics and Biomedical Engineering, Tehran University of Medical Sciences, Tehran, Iran
e-mail: mohammadreza_ay@tums.ac.ir

A. Akbarzadeh · M. R. Ay · A. Ahmadian
Medical Imaging Systems Group, Research Center for Molecular and Cellular Imaging, Tehran University of Medical Sciences, Tehran, Iran

M. R. Ay
Research Institute for Nuclear Medicine, Tehran University of Medical Sciences, Tehran, Iran

H. Zaidi
Division of Nuclear Medicine and Molecular Imaging, Geneva University Hospital, 1211 Geneva, Switzerland
e-mail: habib.zaidi@hcuge.ch

H. Zaidi
Geneva Neuroscience Center, Geneva University, 1205 Geneva, Switzerland

H. Zaidi
Department of Nuclear Medicine and Molecular Imaging, University Medical Center Groningen, University of Groningen, 9700 RB Groningen, Netherlands

## Introduction

Over the past two decades, with the advent of correlative imaging, the role of hybrid technologies has been enhanced in diagnostic imaging. Clinical diagnosis, staging and

assessment of response to therapy, which impact therapeutic options and patient management highly depend on the information provided by imaging technologies. Both structural (CT, MRI) and functional (PET, SPECT, fMRI, DWI) imaging or a combination of both modalities are used clinically and have proven to be useful for the decision-making process and for predicting outcome [1, 2]. The widespread acceptance of PET/CT in clinical setting substantiated that the availability of spatially aligned complementary information compensates for the shortcomings of one modality with the strength of the other [3]. The advantages of PET/CT over its mono-modal counterparts and its role in diagnostic and therapeutic radiology planted the seed of idea to combine PET molecular imaging with high soft-tissue contrast MRI [4–6].

One of the most challenging issues of quantitative PET imaging is attenuation of annihilation photons through their pathway. Attenuation correction requires the availability of the attenuation distribution which accounts for the distribution of attenuating properties of biological tissues. Besides the value of correlated structural information for localization of metabolic abnormalities, the CT component of PET/CT provides the attenuation map to feed the attenuation correction process [7, 8]. On the other hand, the derivation of the attenuation map from MR images is inherently difficult since the MR signal correlates with proton densities and tissue relaxation properties, rather than with electron density and as such it is not directly related to attenuation density [9].

Several techniques have been suggested to derive an attenuation map from MR images [10]. Segmentation-based methods generate an attenuation map by classification of MR images into several classes followed by assignment of predefined attenuation coefficients to various tissue types. Since the segmentation of bones from MR images acquired using conventional sequences is a difficult task, segmentation-based approaches fail to include bones in the attenuation map. A simplified method suitable for clinical whole-body imaging suggested the classification of whole-body images into only three classes (air, soft tissue and lung), which has been implemented on commercial PET/MRI scanners [11, 12]. Another technique considers a 4-class attenuation map (air, lungs, fat, and soft tissue), which requires the acquisition of a 2-point Dixon MR sequence [13]. The method consequently ignores bony structures which are filled with soft-tissue-equivalent medium. Few studies reported on the use of dedicated MR sequence (e.g. ultrashort echo time, UTE) to label bony structures that will likely play a pivotal role for the accurate derivation of attenuation maps from MR images on PET/MR systems [14–17].

The issue of using segmented attenuation maps and its impact on quantitative accuracy has been addressed in a number of studies in the realm of PET/CT [18, 19]. However, these studies still did not address the specificities of PET/MR. Most MR-based attenuation-correction techniques ignore bones owing to the inherent difficulties of bone segmentation from conventional MR sequences. Martinez-Moller et al. [13] recognized that ignoring bone had an impact on lesion quantification, but this impact was small for all lesions, even those located in the pelvic bone and lumbar vertebrae. The largest standardized uptake value (SUV) change (<15 % on average) were reported in lesions located in the bone [11, 13, 20]. However, the influence of bone could be higher in neurologic studies because of the skull through which photons must pass before reaching the detectors [21]. Most previous studies reported that this bias does not affect the clinical interpretation by experienced radiologists.

Concurrent with our group, recently Keereman et al. [22] specifically focused on the error associated with the use of different tissue classes when segmented attenuation correction is applied by means of simulations using the XCAT phantom. Although this study shed light on some issues related to the impact of tissue classes, it has some limitations because of the lack of realistic clinical studies. As a matter of fact, the inclusion of clinical studies strengthens the conclusions reached in more complex situations. In this work, we evaluate the impact of considering hard bone and soft bone on the accuracy of MRAC of PET data using simulation studies of the XCAT phantom and clinical studies.

## Materials and methods

### Input data

#### *XCAT phantom studies*

The XCAT (4D extended cardiac-torso) phantom was used to simulate 3D distributions of activity and attenuation coefficients typical of whole-body PET/CT studies. This phantom was specifically developed for realistic simulation of human anatomy and physiology for nuclear medicine studies [23, 24]. The phantom considers the motion associated with both respiratory and cardiac motion. To isolate the evaluation of MRAC from motion artifacts, we performed a static simulation.

This phantom in fact resembles a database that accepts an input file containing information pertaining to anatomic height, weight, gender and the amount of activity for each organ to create two sets of 3D images: (1) activity map based on a predefined list of activities in the input file and (2) the corresponding attenuation map for the specified energy (511 keV for PET). We created a male subject

having a weight of 85 kg and height of 190 cm. The activity assigned to each region was devised using a combination of clinical PET studies and data available in the literature for whole-body FDG studies [25, 26]. The matrix size of the phantom was 128 × 128 × 461 containing voxels of size 4 × 4 × 4 $mm^3$.

*Clinical studies*

Whole-body $^{18}$F-FDG PET/CT images of 10 patients were acquired on the Biograph 16 PET/CT scanner (Siemens Healthcare, Erlangen, Germany). PET images were acquired with a slice thickness of 5 mm and pixel size of 4.07 × 4.07 $mm^2$ and dimensions of 168 × 168 × 300–400. A low-dose CT scan was performed on CT subsystem of PET/CT for attenuation-correction purposes. It should be noted that the clinical studies used in this work lacked the presence of representative lesions in regions we wanted to focus on (lesions located in different parts of body). As such, our choice was to manually insert lesions in these clinical PET studies according to guidelines provided by nuclear medicine physicians. This retrospective study was approved by the local ethical committee and informed consents were obtained.

## Simulations

*Simulation of lesions*

Realistic lesions were manually placed inside the body or bones paying special attention to mimic typical sizes and uptake of tumors. The lesions consisted of elliptical ROIs with three different diameters and realistic SUVs [27]. The diameter was randomly determined in the range of 10–50 mm. Similarly, the location was randomly selected inside the body as well as osseous regions (focusing on osteo-metastatic lesions). The range of SUVs typical of malignant disease was determined from the literature [28]. The SUV for each lesion was randomly chosen to be in the range [2.5–5], indicating malignancy. The idea is to link potential underestimation of SUV consequent to the use of MR-guided attenuation correction with their clinical misinterpretation as benign. Over 380 lesions were inserted in randomly selected bony regions, whereas over 800 lesions were inserted in random locations in the body of the 10 clinical studies. It should be noted that simulated lesions were inserted in both clinical and phantom studies.

*PET data simulation and image reconstruction*

Analytic simulation is a rapid technique for simulation of PET data. Annihilation photons traverse tissues having different attenuation coefficients and are attenuated through their pathways. Compton scattering was not considered since it was reported to have a minor impact on the results for the purpose of this study [22]. The activity and attenuation maps are used as input to the simulation process, which consists of a forward projection operator taking into account photon attenuation and the genuine geometry of the PET scanner (Siemens Biograph 16 HireZ). Poisson noise was added to the simulated projection data. The simulated PET data were reconstructed using OSEM iterative algorithm (8 subsets and 4 iterations) by means of the STIR image reconstruction library [29]. It should be noted that for clinical studies, the attenuation map is generated using the bilinear energy mapping technique used on the majority of commercial PET/CT scanners [30].

As discussed earlier, the main aim of this study is to assess the effect of using different tissue classifications for generation of the attenuation map. Therefore, the attenuation map is classified into three tissue classes (air, lungs and soft tissue), four tissue classes (air, lungs, soft tissue and cortical bones) and five tissue classes (air, lungs, soft tissue, cortical bones and spongeous bones). Image segmentation was performed using the Insight Toolkit (ITK) object-oriented image processing library [31]. The attenuation map used as input to simulations was considered as reference. The threshold used and assigned attenuation coefficients are summarized in Table 1.

Figure 1 shows a flowchart of the simulation process. The three main steps are explained in more detail as follows:

1. Attenuated PET data are produced using the original activity map and corresponding reference attenuation map. For clinical studies, the actual PET image of each patient was considered as activity map, whereas the attenuation map was derived from its corresponding CT image using bilinear energy mapping.
2. The attenuated emission sinogram resulting from the former stage is corrected for attenuation using the four attenuation maps (3-class, 4-class, 5-class and reference).
3. The sinogram resulting from step #2 is reconstructed using OSEM iterative reconstruction algorithm to provide the corrected PET image.
4. The attenuation-corrected PET image is then compared to the original image and the relative error calculated.

## Quantitative image analysis

The relative error for phantom studies was calculated through voxel-by-voxel subtraction of the reconstructed PET image from the reference image and dividing it by the latter using the following equation:

**Table 1** Thresholds used for segmentation of the attenuation map and CT image into different tissue classes together with the assigned linear attenuation coefficient

| | Class 2 | Class 3 | Class 4 | Class 5 |
|---|---|---|---|---|
| XCAT μ-map | | | | |
| Three-class | $I \leq 0.096 \leftarrow 0.0286$ | $0.096 < I \leftarrow 0.096$ | – | – |
| Four-class | $I \leq 0.096 \leftarrow 0.0286$ | $0.096 < I \leq 0.134 \leftarrow 0.096$ | $0.134 < I \leftarrow 0.134$ | – |
| Five-class | $I \leq 0.096 \leftarrow 0.0286$ | $0.096 < I \leq 0.101 \leftarrow 0.096$ | $0.101 < I \leq 0.134 \leftarrow 0.101$ | $0.134 < I \leftarrow 0.134$ |
| CT image | | | | |
| Three-class | $I \leq -200 \leftarrow 0.0286$ | $-200 < I \leftarrow 0.096$ | – | – |
| Four-class | $I \leq -200 \leftarrow 0.0286$ | $-200 < I \leq 300 \leftarrow 0.096$ | $300 < I \leftarrow 0.134$ | – |
| Five-class | $I \leq -200 \leftarrow 0.0286$ | $-200 < I \leq 100 \leftarrow 0.096$ | $100 < I \leq 300 \leftarrow 0.101$ | $300 < I \leftarrow 0.134$ |

One class corresponds to image background (air) is not mentioned here

The following pattern was used. XCAT μ-maps: lower thr($cm^{-1}$) < I < upper thr($cm^{-1}$) ← assigned value($cm^{-1}$). CT images: lower thr (HU) < I < upper thr (HU) ← assigned value ($cm^{-1}$)

$$\text{Relative error} = \frac{\text{Measured activity} - \text{Original activity}}{\text{Original activity}} \times 100\ \%. \quad (1)$$

It can be deduced from Eq. (1) that a negative relative error demonstrates that the corrected image underestimates the initial activity, whereas a positive relative error demonstrates that the corrected image overestimates the original activity map.

The correlation coefficient is a statistical parameter that shows the linear dependency of two groups of samples. We calculate the correlation coefficient between PET images obtained using the different attenuation-correction methods and the reference image. When the two samples are linearly correlated, their correlation coefficient approaches 1.

Attenuation correction and image reconstruction were performed using the STIR library [29]. Spherical ROIs corresponding to the location of the simulated lesions were outlined to calculate the SUV for each ROI using the formula:

$$\text{SUV}_{\text{mean/max}} = \frac{(\text{activity concentration in ROI})_{\text{mean/max}}}{\text{Injected activity/body weight}}. \quad (2)$$

Since $\text{SUV}_{\text{max}}$ is very sensitive to noise, the maximum value for each ROI was selected after averaging the considered voxel with its 26 neighbors. Relative $\text{error}_{\text{mean/max}}$ which directly reflects the dispersion of $\text{SUV}_{\text{mean/max}}$ from the original SUV in PET images is calculated using the following formula:

$$\text{Relative error}_{\text{mean/max}} = \frac{\text{SUV}_{\text{mean/max}} - \text{Original SUV}}{\text{Original SUV}} \times\ 100\,\%. \quad (3)$$

It should be noted that a negative relative $\text{error}_{\text{mean/max}}$ reflects an underestimation of $\text{SUV}_{\text{mean/max}}$, whereas a positive relative $\text{error}_{\text{mean/max}}$ reflects an overestimation of $\text{SUV}_{\text{mean/max}}$. In order to assess the effect of using different attenuation maps on clinical interpretation, it was hypothesized that lesions with $\text{SUV}_{\text{max}}$ smaller than 2 (while their original $\text{SUV}_{\text{max}}$ was higher than 2.5) can be considered as benign. The total number of benign lesions for each attenuation-correction method was obtained.

The results of the comparative analysis are shown using box and whisker plots. In these plots, the box shows the median (horizontal line), whereas the lower (Q1) and upper quartiles (Q3) define the 25th and 75th percentiles. The plus sign in the plots indicates the outliers. Outliers in the plot include dubious results which are beyond of 1.5 times the inter-quartile range (Q3–Q1). The whiskers show the maximum and minimum of population after elimination of outliers. The notches display the variability of the median between samples. The width of a notch is computed so that the box plots whose notches do not overlap have different medians at the 5 % significance level. The significance level is based on a normal distribution assumption, but comparisons of medians are reasonably robust for other distributions. Comparing box plot medians is similar to a visual hypothesis test, analogous to the *t* test used for means.

## Results

Figure 2 shows the relative error maps (image depicting the relative error voxel-by-voxel) where voxel values indicate the percentage of relative errors (Eq. 1). The results seem to indicate that neglecting bone causes a significant error. Figure 3 shows the box and whisker plots reflecting statistical analysis of the relative error for various regions of the XCAT phantom. The samples shown in Fig. 3a were selected from various parts of the body. Similarly, samples selected from bones and bone marrow are shown in Fig. 3b.

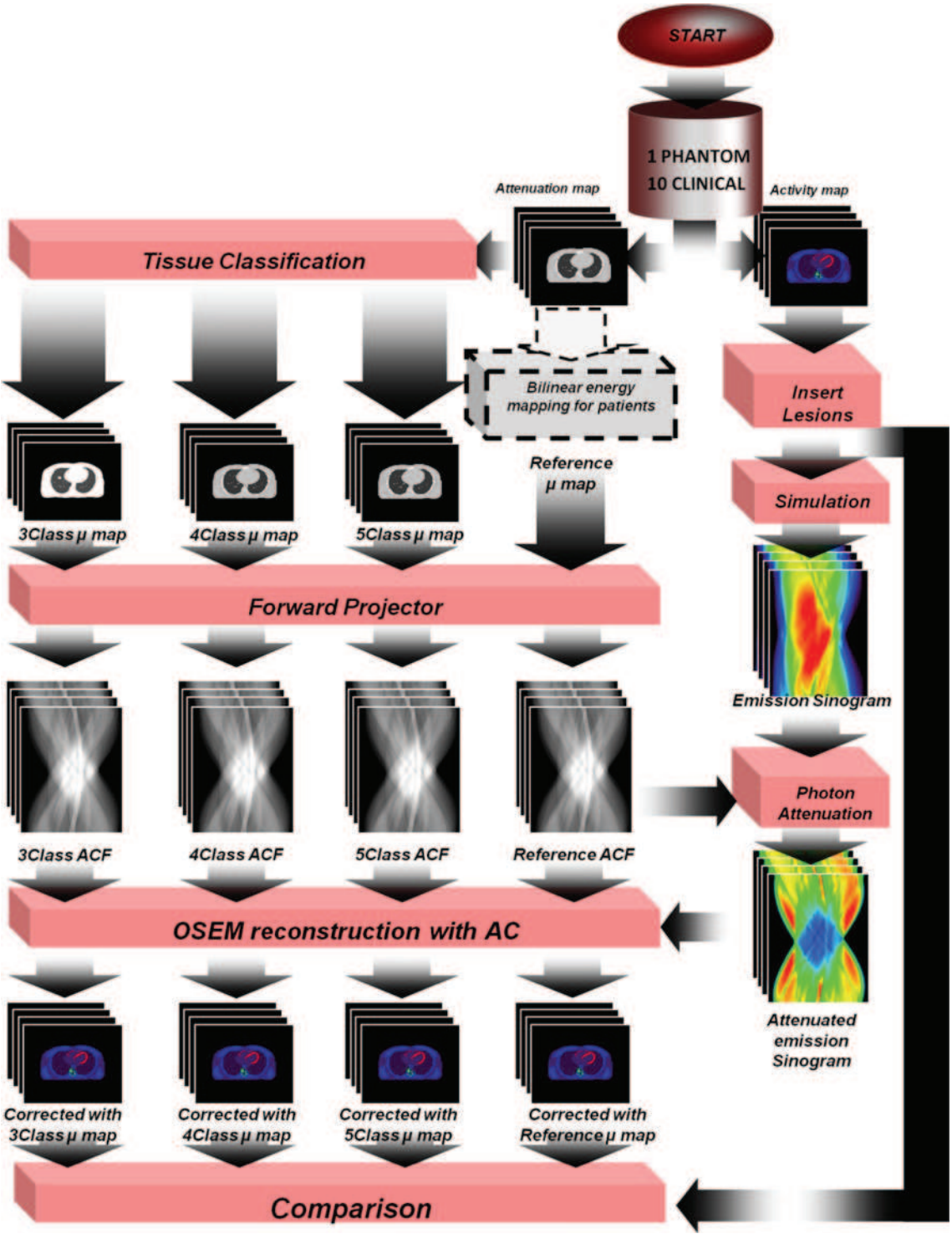


**Fig. 1** Flowchart of the overall simulation procedure used for phantom and clinical studies

The reconstructed images of the XCAT phantom corrected for attenuation using segmented and reference attenuation maps were compared with the phantom's original activity distribution. The average error (Relative $\text{error}_{\text{mean}}$) for each lesion was calculated for various organs and is illustrated in Fig. 4. Figure 5 plots the correlation coefficients between clinical PET images obtained using the various attenuation-correction techniques and the original images. The closer the correlation coefficient to identity, the better the correlation between the ground truth and the corresponding attenuation-correction procedure. It was observed that for all simulated phantoms and clinical

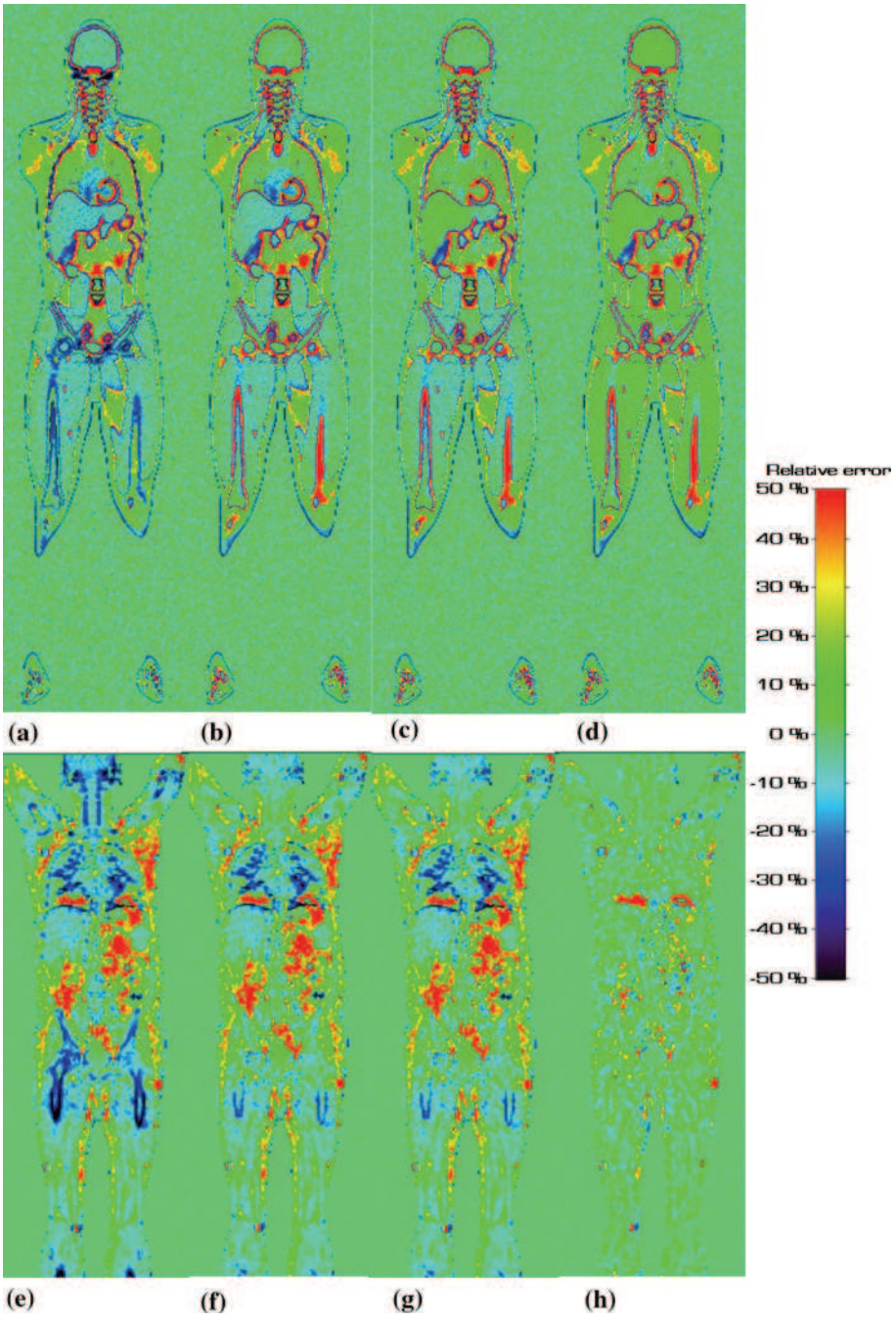


**Fig. 2** Relative error maps resulting from attenuation correction of phantom (**a**–**d**) and clinical (**e**–**h**) studies. Attenuation correction uses: three-class attenuation map (**a**, **e**), four-class attenuation map (**b**, **f**), five-class attenuation map (**c**, **g**), reference attenuation map (**d**) for the phantom study, and bilinear attenuation map (**h**) for the clinical study

studies, increasing the number of classes will definitely increase the accuracy of attenuation correction. Statistical analysis proved that there is statistically significant difference between the attenuation-correction techniques.

Figure 6a, b shows box and whisker plots for relative $error_{mean}$ and relative $error_{max}$ for ROI-based analysis of about 386 lesions located in bones simulating osteo-metastatic lesions for 10 patients. It can be seen that the bilinear CT-based attenuation correction underestimates $SUV_{max}$ by 13.4 % and slightly overestimates ($\sim$0.4 %) $SUV_{mean}$. However, the attenuation-correction methods using 3-class, 4-class and 5-class classified attenuation maps largely underestimate both $SUV_{mean}$ and $SUV_{max}$. Figure 6c, d shows relative $error_{mean}$ and relative $error_{max}$ for lesions in the body excluding bones. These lesions were simulated to contain equal $SUV_{mean}$ and $SUV_{max}$ randomly from 2 up to 5. Over 800 lesions were located in 10 patients. Figure 6c, d indicates that the bilinear CT-based attenuation-correction technique causes 3.6 % underestimation of $SUV_{max}$ and 6.3 % underestimation of $SUV_{mean}$. However, attenuation-correction methods using 3-class, 4-class and 5-class attenuation maps demonstrate larger underestimations of both $SUV_{max}$ and $SUV_{mean}$.

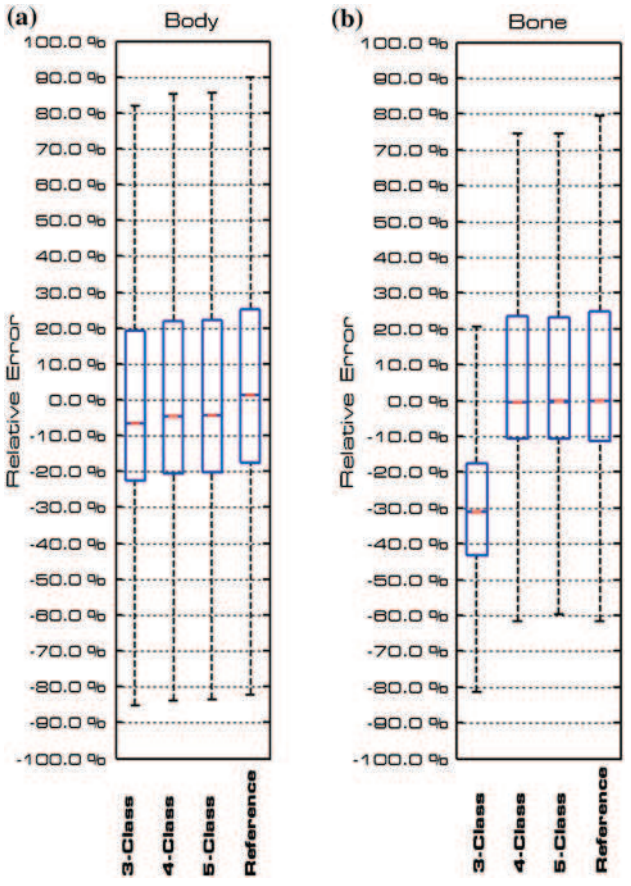


**Fig. 3** *Box and whisker plots* illustrating the statistical analysis of the error image for the XCAT phantom: **a** samples selected from body, **b** samples selected from bones and bone marrow

Table 2 summarizes the number of lesions inside bones or the body classified as benign ($SUV_{max} < 2$) while their initial $SUV_{max}$ was higher than 2.5. Lesions with different uptakes were counted separately. The percentage of misinterpreted lesions is also reported.

## Discussion

The main objective of this work is to quantify the impact of using different number of tissue classes on the accuracy of MR-guided attenuation correction of PET data. This assessment consisted of simulated phantoms using the XCAT model and clinical studies. The relative error depicted in Fig. 3 as box and whisker plot was calculated voxel by voxel. The large number of voxels and their different characteristics explains the wide range of the relative error distribution. The wide boxes and whiskers make the comparison of the different attenuation-correction methods difficult. On the other hand, owing to the large number of voxels, the margin of statistical insignificance (confidence interval) falls down. This enables direct comparison of different techniques. The phantom study substantiates the hypothesis that the higher the number of tissue classes in the attenuation map, the more the recovered activity approaches the original activity for lesions located in the body (Fig. 3a). When using the reference attenuation map for AC, the median of the relative error for all voxels of the body is equal to 1.34 ± 0.04 % (Fig. 3a). The value 0.04 % is the confidence interval for a significance level of 95 %. The use of 5-class, 4-class and 3-class attenuation maps resulted in progressively increasing underestimation of tracer uptake in attenuation-corrected PET images of the XCAT phantom, respectively.

Figure 3b shows another sight of using different attenuation maps. The evaluation of the impact of a different number of tissue classes for generation of the attenuation map around bones and bone marrows highlights the fact that neglecting bone will lead to a larger underestimation of tracer uptake in PET images. Attenuation correction using a 3-class attenuation map, which ignores all bones and harder anatomical structures, underestimates tracer uptake by 31.05 ± 0.05 % in bones and their neighborhoods. Other methods that consider bone result in smaller relative errors (under 1 %) in bony structures.

Figure 3 corroborates the fact that the relative error for the whole-body increases significantly as the number of classes decreases. On the other hand, ignoring bones in the 3-class attenuation map causes serious errors in bony structures, whereas taking bone into account in the derivation of the attenuation map reduces the relative error. Figure 4 demonstrates that the SUV for lesions located inside bones is largely underestimated by about 25 % for

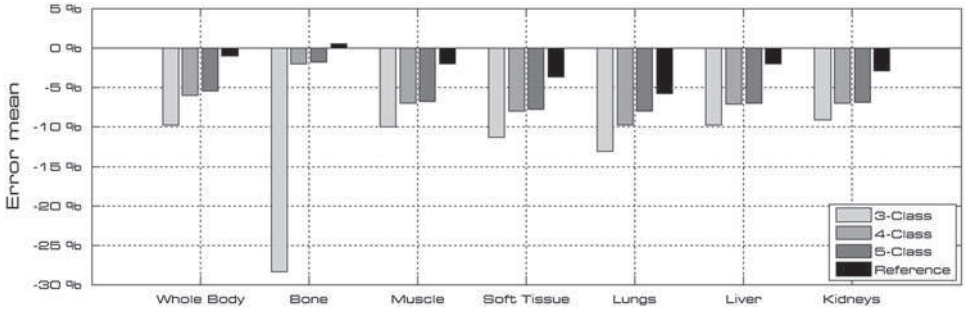


**Fig. 4** Average relative $error_{mean}$ for lesions inside various parts of the XCAT phantom

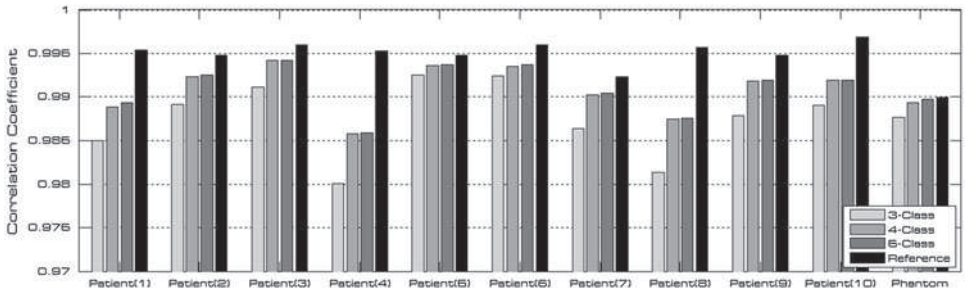


**Fig. 5** Correlation coefficients calculated through voxel-by-voxel statistical analysis of the original and corrected images for the XCAT phantom and 10 clinical studies considered

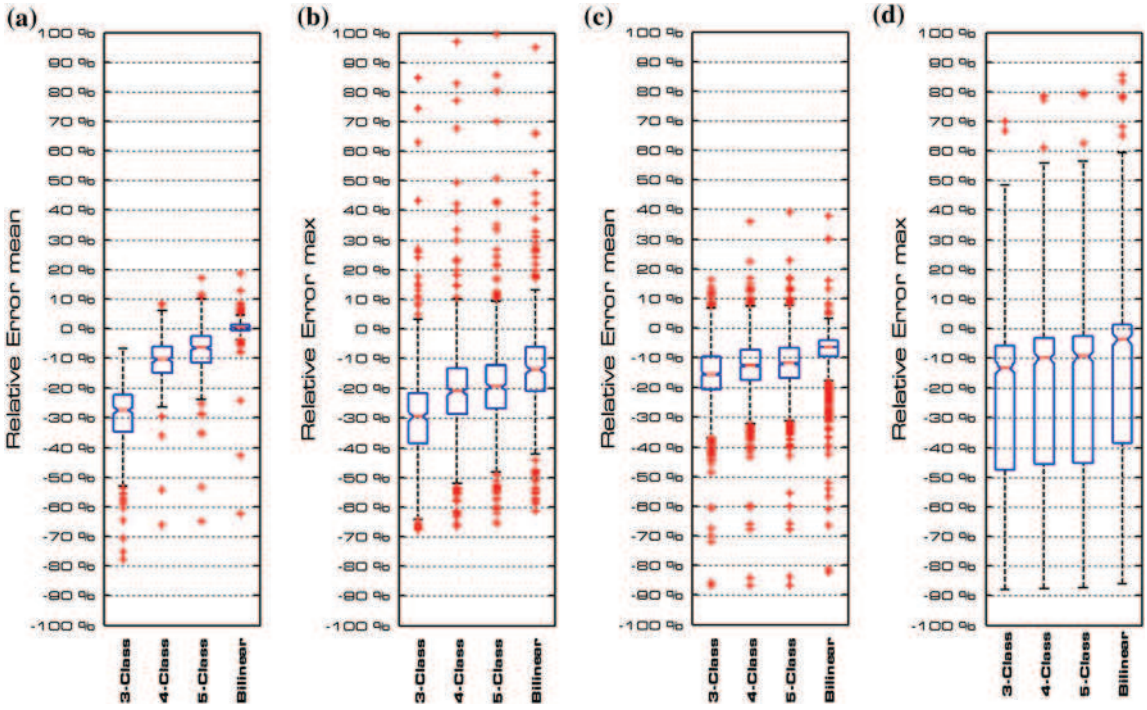


**Fig. 6** *Box and whisker plots* illustrating relative $error_{mean}$ and relative $error_{max}$ calculated for simulated lesions in bones (**a**, **b**) and in the body (**c**, **d**) for all patients

**Table 2** Impact of using different tissue classes in the attenuation map on lesions' uptake

| Reference $SUV_{max}$ | | Number of lesions with $SUV_{max} < 2$ | | | | Total | Percentage (%) of lesions classified as benign ($SUV_{max} < 2$) | | | |
|---|---|---|---|---|---|---|---|---|---|---|
| | | 3-Class | 4-Class | 5-Class | Bilinear | | 3-Class | 4-Class | 5-Class | Bilinear |
| Bone | 2.5–3 | 36 | 8 | 6 | 1 | 64 | 56.2 | 12.5 | 9.4 | 1.6 |
| | 3–4 | 55 | 15 | 10 | 5 | 167 | 32.9 | 9.0 | 6.0 | 3.0 |
| | 4–5 | 35 | 10 | 5 | 1 | 149 | 23.5 | 6.7 | 3.4 | 0.7 |
| | > 5 | 2 | 1 | 1 | 0 | 6 | 33.3 | 16.7 | 16.7 | 0.0 |
| Body | 2.5–3 | 66 | 17 | 13 | 3 | 140 | 47.14 | 12.1 | 9.3 | 2.1 |
| | 3–4 | 9 | 7 | 4 | 0 | 352 | 2.56 | 2.0 | 1.1 | 0.0 |
| | 4–5 | 0 | 0 | 0 | 0 | 362 | 0.00 | 0.0 | 0.0 | 0.0 |
| | >5 | 0 | 0 | 0 | 0 | 19 | 0.00 | 0.0 | 0.0 | 0.0 |

All simulated lesions had an initial $SUV_{max}$ >2.5. Lesions with $SUV_{max}$ <2 after attenuation correction were classified as benign

the 3-class attenuation map. The difference between PET images corrected for attenuation using the reference attenuation map and the original images is likely due to errors associated with organ boundaries.

The correlation coefficient between PET images corrected for attenuation correction using the different and original image is another relevant parameter for comparative analysis (Fig. 5). As the number of classes in the attenuation map increases, the correlation coefficient becomes closer to one confirming the hypothesis that increasing the number of classes will improve the accuracy of attenuation correction. Statistical hypothesis testing was carried out to assess whether two correlations have different strengths. Since the number of samples was relatively high, all correlation coefficients are different with a significance level of 99 %. It should be noted that we assumed that all samples are normally distributed for statistical testing (the normality of samples was verified using Chi-square test).

Relative $error_{mean/max}$ for $SUV_{mean/max}$ index is another parameter for assessment of different attenuation-correction techniques used for clinical simulation studies. It should be mentioned that Relative $error_{max}$ calculated from $SUV_{max}$ is highly sensitive to statistical noise since it reflects the value of only one voxel. The latter is, however, less dependent on the shape, size and location of the ROI. Notwithstanding, $SUV_{max}$ suffers from inferior reproducibility in comparison with $SUV_{mean}$ [32].

Figure 6a, b show relative $error_{mean}$ and relative $error_{max}$ calculated over 386 ROIs for the 10 patients included in this study. Both metrics support the fact that a higher number of classes improves the accuracy of the attenuation-correction procedure. This is in agreement with the previous phantom study. However, a close look at the results reported in Table 3 indicates that relative $error_{max}$ (for simulated osteo-metastatic lesions) are not significantly different with a significance level of 95 % when using 4-class and 5-class attenuation maps. This is in line with observations made for the phantom study (Fig. 3b). The reason behind is that the 5-class and 4-class attenuation maps are slightly different in their contents since the 4-class attenuation map considers only hard bones as an individual class, whereas a 5-class attenuation map also considers soft bones.

Figure 6c, d show the results for simulated lesions in the body. Similar behavior is observed when increasing the number of classes in terms of reducing relative $error_{mean}$ and relative $error_{max}$. Table 3 shows the median of relative $error_{mean}$ and relative $error_{max}$ for each group of ROIs along with their confidence interval for 95 % confidence level. There is a small difference between relative $error_{mean}$ and relative $error_{max}$ when using the various attenuation-correction techniques using 4-class and 5-class attenuation maps. Consequently, although considering soft bones as a distinct class in the attenuation map slightly improves the accuracy of attenuation correction, it is not as vital as including hard bones as a separate class. This is further demonstrated in Table 2 where it can be observed that ignoring hard bones in the attenuation map results in a larger rate of misinterpretations than ignoring soft bones. For clinical studies, considering bone in osteo-metastatic lesions decreases relative $error_{mean}$ and relative $error_{max}$ by $17.19 \pm 2.2$ % and $8.58 \pm 0.4$ %, respectively, when comparing 3-class with 4-class attenuation maps. For lesions located in the body, relative $error_{mean}$ and relative $error_{max}$ decrease by 2.9 and 3 %, respectively.

**Table 3** Summary of median and corresponding 95 % confidence interval calculated over all simulated lesions in bones and the body of the patients when using different attenuation-correction procedures

| | AC technique | Notch-low (%) | Median (%) | Notch-high (%) | Confidence interval (%) |
|---|---|---|---|---|---|
| *Body* | | | | | |
| $Error_{mean}$ | 3-class | −15.83 | −15.37 | −14.90 | 0.93 |
| | 4-class | −12.91 | −12.49 | −12.07 | 0.84 |
| | 5-class | −12.34 | −11.92 | −11.51 | 0.83 |
| | Bilinear | −6.57 | −6.34 | −6.11 | 0.46 |
| $Error_{max}$ | 3-class | −14.78 | −13.01 | −11.24 | 3.54 |
| | 4-class | −11.78 | −9.99 | −8.19 | 3.59 |
| | 5-class | −11.23 | −9.41 | −7.60 | 3.62 |
| | Bilinear | −5.31 | −3.63 | −1.95 | 3.35 |
| *Bones* | | | | | |
| $Error_{mean}$ | 3-class | −28.36 | −27.27 | −26.19 | 2.17 |
| | 4-class | −11.17 | −10.41 | −9.65 | 1.52 |
| | 5-class | −7.20 | −6.44 | −5.69 | 1.52 |
| | Bilinear | 0.17 | 0.35 | 0.54 | 0.37 |
| $Error_{max}$ | 3-class | −30.72 | −29.34 | −27.97 | 2.76 |
| | 4-class | −22.14 | −20.90 | −19.65 | 2.49 |
| | 5-class | −20.50 | −19.34 | −18.18 | 2.32 |
| | Bilinear | −14.62 | −13.43 | −12.25 | 2.36 |

It was observed for both phantom and clinical simulation studies, that the actual or reference attenuation map (bilinear conversion curve) produces small errors (Figs. 4, 6). In this case, since the reference images were forward projected considering photon attenuation and then attenuation corrected using the same attenuation map, error-free reconstruction is expected. However, in practice the reconstruction process suffers from numerical instability especially in sharp boundaries which leads to such errors.

Different values for SUV underestimation in bone lesions have been reported in the literature ranging between

5 and 15 % [11, 13, 33] and going up to 23 % [34]. Simulation studies using the XCAT phantom reported biases of up to 17.5 % [22], whereas our assessment led to a bias of $28.36 \pm 1.08$ % for $SUV_{mean}$ and $30.72 \pm 1.38$ % for $SUV_{max}$ [35]. Our results suggest higher relative errors compared to previous works. One possible reason could be the way the lesions were simulated. Indeed, the lesions were inserted inside bones and none of them was partially outside the bones. The size of lesions was also relatively small which can be another reason for the large deviations.

According to nuclear medicine physicians, such underestimation might impact their interpretation having as consequence mis-staging of tumors with low SUV in some cases, while there is potential of misjudgment when assessing response to treatment for tumors with relatively high SUV.

Table 2 shows that for bony tumors, over 50 % of the lesions having an initial uptake from 2.5 to 3 could be interpreted as benign lesions when using a 3-class attenuation map. For lesions with higher uptake, the percentage of misinterpretation falls down to 33 % ($3 < SUV < 4$) and 23 % ($4 < SUV < 5$). The number of misinterpreted lesions in the body with an $SUV > 3$ drastically falls down owing to the fact that the error for body lesions is lower in comparison with bony lesions.

The use of a sharp SUV cut-off threshold to discriminate between benign and malignant lesions has been widely discussed in the literature and still remains a matter of debate. Different ranges of $SUV_{max}$ for various tumor entities have been proposed [36–38]. Owing to the variability in PET scanner design and performance parameters, acquisition and processing protocols and study populations, it is impossible to draw an unambiguous conclusion about a common SUV cut-off threshold. A recent study [39] has shown that the range of $SUV_{max}$ for benign tumors slightly overlaps with that for malignant tumors. As such, our approach bears some inherent limitations in this respect.

According to our previous experience [8, 40–42], we believe that a study design involving the use of human observers with a ranking procedure to assess the impact of various attenuation-correction strategies on visual quality of PET images is not the best strategy given the small visual changes noticeable on clinical images. Therefore, we relied on quantitative changes in PET images based on the hypothesis that underestimations of SUV resulting from the use of MR-guided attenuation correction could result in misinterpretations of malignant lesions as benign.

## Conclusion

We evaluated the impact of using different number of tissue classes in MR segmentation-based attenuation correction in PET/MRI. We particularly focused on the controversial effect of neglecting bone and the improvement brought by considering hard and soft bones. Overall, it has been shown that considering bone improves the accuracy of MR-guided attenuation correction. The quantitative assessment revealed a 50 % underestimation of SUVs ranging between 2.5 and 3 owing to ignoring bone, which might cause misinterpretation of bone tumor staging. Our study substantiates that the choice of the number of tissue classes has a significant impact on the clinical interpretation of osteo-metastatic lesions and needs to be optimized for hybrid PET/MR technologies.

**Acknowledgments** This work was supported by Tehran University of Medical Sciences under Grant No. 10934, the Swiss National Science Foundation under grants SNSF 31003A-135576, 33CM30-124114, and Geneva Cancer League. The authors are indebted to Dr. Paul Segars for providing the XCAT phantom.

## References

1. Schmidt GP, Schmid R, Hahn K, Reiser MF. Whole-body MRI and PET/CT in tumor diagnosis. Der Radiologe. 2004;44:1079–87.
2. Seemann MD, Meisetschlaeger G, Gaa J, Rummeny EJ. Assessment of the extent of metastases of gastrointestinal carcinoid tumors using whole-body PET, CT, MRI, PET/CT and PET/MRI. Eur J Med Res. 2006;11:58–65.
3. Antoch G, Vogt FM, Freudenberg LS, Nazaradeh F, Goehde SC, Barkhausen J, et al. Whole-body dual-modality PET/CT and whole-body MRI for tumor staging in oncology. JAMA. 2003;290:3199–206.
4. Antoch G, Bockisch A. Combined PET/MRI: a new dimension in whole-body oncology imaging? Eur J Nuc Med Mol Imaging. 2009;36(Suppl 1):S113–20.
5. Heiss W-D. The potential of PET/MR for brain imaging. Eur J Nuc Med Mol Imaging. 2009;36(Suppl 1):S105–12.
6. Zaidi H, Del Guerra A. An outlook on future design of hybrid PET/MRI systems. Med Phys. 2011;38:5667.
7. Kinahan PE, Hasegawa BH, Beyer T. X-ray-based attenuation correction for positron emission tomography/computed tomography scanners. Semin Nucl Med. 2003;33:166–79.
8. Ay MR, Shirmohammad M, Sarkar S, Rahmim A, Zaidi H. Comparative assessment of energy-mapping approaches in CT-based attenuation correction for PET. Mol Imaging Biol. 2011;13:187–98.
9. Zaidi H. Is MRI-guided attenuation correction a viable option for dual-modality PET/MR imaging? Radiology. 2007;244:639–42.
10. Hofmann M, Pichler B, Schölkopf B, Beyer T. Towards quantitative PET/MRI: a review of MR-based attenuation correction techniques. Eur J Nuc Med Mol Imaging. 2009;36(Suppl 1):S93–104.
11. Schulz V, Torres-Espallardo I, Renisch S, Hu Z, Ojha N, Börnert P, et al. Automatic, three-segment, MR-based attenuation correction for whole-body PET/MR data. Eur J Nucl Med Mol Imaging. 2011;38:138–52.
12. Zaidi H, Ojha N, Morich M, Griesmer J, Hu Z, Maniawski P, et al. Design and performance evaluation of a whole-body Ingenuity TF PET-MRI system. Phys Med Biol. 2011;56:3091–106.
13. Martinez-Moller A, Souvatzoglou M, Delso G, Bundschuh RA, Chefd'hotel C, Ziegler SI, et al. Tissue classification as a

potential approach for attenuation correction in whole-body PET/MRI: evaluation with PET/CT data. J Nucl Med. 2009;50:520–6.
14. Keereman V, Fierens Y, Broux T, De Deene Y, Lonneux M, Vandenberghe S. MRI-based attenuation correction for PET/MRI using ultrashort echo time sequences. J Nucl Med. 2010;51:812–8.
15. Catana C, van der Kouwe A, Benner T, Michel CJ, Hamm M, Fenchel M, et al. Toward implementing an MRI-based PET attenuation-correction method for neurologic studies on the MR-PET brain prototype. J Nucl Med. 2010;51:1431–8.
16. Berker Y, Franke J, Salomon A, Palmowski M, Donker HC, Temur Y, et al. MRI-based attenuation correction for hybrid PET/MRI systems: A 4-class tissue segmentation technique using a combined Ultrashort-Echo-Time/Dixon MRI sequence. J Nucl Med. 2012;53:796–804.
17. Johansson A, Karlsson M, Nyholm T. CT substitute derived from MRI sequences with ultrashort echo time. Med Phys. 2011;38:2708–14.
18. Kinahan PE, Townsend DW, Beyer T, Sashin D. Attenuation correction for a combined 3D PET/CT scanner. Med Phys. 1998;25:2046–53.
19. Visvikis D, Costa DC, Croasdale I, Lonn AH, Bomanji J, Gacinovic S, et al. CT-based attenuation correction in the calculation of semi-quantitative indices of [18F]FDG uptake in PET. Eur J Nucl Med Mol Imaging. 2003;30:344–53.
20. Hu Z, Ojha N, Renisch S, Schulz V, Torres I, Pal D, et al. MR-based attenuation correction for a whole-body sequential PET/MR system. In: M11-6, editor. IEEE nuclear science symposium and medical imaging conference. 25–31 October 2009, Orlando (FL), USA: IEEE, 2009, pp. 3508–12.
21. Zaidi H, Montandon M-L, Slosman DO. Magnetic resonance imaging-guided attenuation and scatter corrections in three-dimensional brain positron emission tomography. Med Phys. 2003;30:937–48.
22. Keereman V, Holen RV, Mollet P, Vandenberghe S. The effect of errors in segmented attenuation maps on PET quantification. Med Phys. 2011;38:6010–9.
23. Segars WP, Mahesh M, Beck TJ, Frey EC, Tsui BMW. Realistic CT simulation using the 4D XCAT phantom. Med Phys. 2008;35:3800–8.
24. Segars WP, Sturgeon G, Mendonca S, Grimes J, Tsui BM. 4D XCAT phantom for multimodality imaging research. Med Phys. 2010;37:4902–15.
25. Raylman RR, Kison PV, Wahl RL. Capabilities of two- and three-dimensional FDG-PET for detecting small lesions and lymph nodes in the upper torso: a dynamic phantom study. Eur J Nucl Med. 1999;26:39–45.
26. Zasadny KR, Wahl RL. Standardized uptake values of normal tissues at PET with 2-[fluorine-18]-fluoro-2-deoxy-D-glucose: variations with body weight and a method for correction. Radiology. 1993;189:847–50.
27. Thie JA. Understanding the standardized uptake value, its methods, and implications for usage. J Nucl Med. 2004;45:1431–4.
28. Valk PE, Delbeke D, Bailey DL, editors. Positron Emission Tomography: Clinical Practice. Chapter 5 ed. London: Springer; 2006
29. Thielemans K, Tsoumpas C, Mustafovic S, Beisel T, Aguiar P, Dikaios N, et al. STIR: software for tomographic image reconstruction release 2. Phys Med Biol. 2012;57:867–83.
30. Carney JP, Townsend DW, Rappoport V, Bendriem B. Method for transforming CT images for attenuation correction in PET/CT imaging. Med Phys. 2006;33:976–83.
31. Yoo TS, Ackerman MJ, Lorensen WE, Schroeder W, Chalana V, Aylward S, et al. Engineering and algorithm design for an image processing Api: a technical report on ITK-the Insight Toolkit. Stud Health Technol Inform. 2002;85:586–92.
32. Nahmias C, Wahl LM. Reproducibility of standardized uptake value measurements determined by 18F-FDG PET in malignant tumors. J Nucl Med. 2008;49:1804–8.
33. Hofmann M, Bezrukov I, Mantlik F, Aschoff P, Steinke F, Beyer T, et al. MRI-based attenuation correction for whole-body PET/MRI: quantitative evaluation of segmentation- and Atlas-based methods. J Nucl Med. 2011;52:1392–9.
34. Samarin A, Burger C, Wollenweber SD, Crook DW, Burger IA, Schmid DT, et al. PET/MR imaging of bone lesions—implications for PET quantification from imperfect attenuation correction. Eur J Nucl Med Mol Imaging. 2012;39:1154–60.
35. Akbarzadeh A, Ay MR, Ahmadian A, Riahi Alam N, Zaidi H. Impact of using different tissue classes on the accuracy of MR-based attenuation correction in PET-MRI. IEEE Nuclear Science Symposium and Medical Imaging Conference (NSS/MIC), 2011, pp. 2524–30.
36. Kim SK, Allen-Auerbach M, Goldin J, Fueger BJ, Dahlbom M, Brown M, et al. Accuracy of PET/CT in characterization of solitary pulmonary lesions. J Nucl Med. 2007;48:214–20.
37. Murakami R, Uozumi H, Hirai T, Nishimura R, Shiraishi S, Ota K, et al. Impact of FDG-PET/CT imaging on nodal staging for head-and-neck squamous cell carcinoma. Int J Radiat Oncol Biol Phys. 2007;68:377–82.
38. Hubner KF, Buonocore E, Gould HR, Thie J, Smith GT, Stephens S, et al. Differentiating benign from malignant lung lesions using "quantitative" parameters of FDG PET images. Clin Nucl Med. 1996;21:941–9.
39. Nguyen NC, Kaushik A, Wolverson MK, Osman MM. Is there a common SUV threshold in oncological FDG PET/CT, at least for some common indications? A retrospective study. Acta Oncol. 2011;50:670–7.
40. Ay M, Zaidi H. Computed Tomography-based attenuation correction in neurological positron emission tomography: evaluation of the effect of X-ray tube voltage on quantitative analysis. Nucl Med Commun. 2006;27:339–46.
41. Ay M, Zaidi H. Assessment of errors caused by x-ray scatter and use of contrast medium when using CT-based attenuation correction in PET. Eur J Nucl Med Mol Imaging. 2006;33:1301–13.
42. Teimourian B, Ay MR, Zafarghandi MS, Ghafarian P, Ghadiri H, Zaidi H. A novel energy mapping approach for CT-based attenuation correction in PET. Med Phys. 2012;39:2078–89.